

Effect of swirl angle on radiation models and spray flame

Alaa Jasim Alshiblawi

*Mechanical Eng, Eng College, University of Al-Qadisiyah, Iraq,
alaajasim797@gmail.com*

Ahmed Abed Al Kadhem Majhool

Mechanical Eng, Eng College, University of Al-Qadisiyah, Iraq.

Abstract

The impacts of thermal radiation at various degrees of main air swirl flow have been numerically simulated, as has the kerosene fuel spray is burned. Used radiation models and the k- ϵ model to simulate turbulent quantities. A model with thorough kerosene combustion dynamics is projected using a statistical model with kerosene fuel-specific model variables. In order to forecast, flow of incident heat on the fuel injector and combustor wall contributions from thermal radiation and the gas phase have both taken into account. The primary flow's swirl has a big impact on the combustor's flow and flame structures. More air is drawn into the flame zone by the higher recirculation at a high swirl, which both shortens the flame and lowers the peak flame temperature while bringing more air to the input plane. As a result, at a high swirl, the radiant heat flow on the peripheral wall diminishes and moves inward toward the inlet plane. However, due to the flame expanding radially, increasing swirl raises the temperature of the combustor wall. The fuel injector is an essential component of the combustor due to the high occurrence radiant high surface temperature and heat flux Considering the proximity the entrance plane of the fire. the injector's maximum temperature rises as the swirl flow increases. On the other hand, strong swirl conditions near the combustor outlet can lead to a more even temperature distribution the exhaust stream. The outcomes of the numerical simulation are contrasted with experimental. The outcomes showed that a swirling angle (40, 50, and 60) provided good results through temperature, incidence radiation, and thermal efficiency.

Keywords: *P1 radiation model, Spray combustion, Discrete coordinate, swirl angle.*

1. INTRODUCTION

Combustors for gas turbines are mostly utilized in different, power generating, and maritime transportation. the air provided by the compressor is entered through various places a gas turbine's combustor's combustor. The main air consists of solely

responsible for oxidizing the fuel, the Secondary air is used to complete the combustion of any remaining species, as well as the dilution air responsible for keeping within metallurgical terms, the gas's temperature as it passes through the turbine limitations. [1]. Through a swirler with either a constant or variable

Nomenclature			
C_p	specific heat ($\text{J kg}^{-1} \text{K}^{-1}$)	<i>Greek symbols</i>	
g_i	gravitational acceleration (m s^{-2})	σ_s	scattering coefficient
k	thermal conductivity ($\text{W m}^{-1} \text{K}^{-1}$)	σ	Stefan-Boltzmann Constant
p	Static pressure ($\text{kg m}^{-1} \text{s}^{-2}$)	$\sigma_{s\lambda}$	spectral scattering coefficient
Pr	Prandtl number	a_λ	spectral absorption coefficient
T	Temperature (K)	Φ_v	Rayleigh dissipation function (kg m^{-3})
U_i	velocity (m s^{-1})	μ	molecular viscosity ($\text{kg m}^{-2}\text{s}^{-2}$)
S_m	mass to gas-phase (kg m^{-3})	ϵ	turbulence dissipation rate
U_p	Droplets velocity (m s^{-1})	G_λ	spectral incident radiation
F_i	momentum force ($\text{kg m}^{-2} \text{S}^{-2}$)	$S_{G\lambda}$	defined source term
h_i	Enthalpy	λ	wavelength
j_i	diffusion flux ($\text{kg m}^{-2} \text{S}$)	α_λ	spectral absorption coefficient
		$I_{b\lambda}$	black body intensity
r_t	turbulent prandtl number	<i>Subscr</i>	
S_h	volumetric heat source ($\text{kg m}^{-2} \text{S}$)	CFD	Computational Fluid Dynamics
S_f	momentum source term ($\text{kg m}^{-2} \text{S}^{-2}$)	DOM	Discrete Ordinate Method
S_G	Radiation source	RTE	Radiation Transfer Equation
K	turbulent kinetic energy	WSGG	Weighted Sum Of Gray Gases Model
		M	
f	mixture fraction	P1	Spherical Harmonic
		PDF	Probability Density Function

vane angle, primary air enters the chamber of combustion. A center zone of recirculation is generated when the flow is given a swirl,

which causes the pressure close to the axis to decrease and creates an unfavorable gradient of pressure. The flame length is reduced, and

the flame's stability is increased, by adding a whirling movement to the intake air. Over the past few decades, extensive. There has been study conducted on the topic of combustion in gas turbines to enhance the combustors' design and performance qualities [2, 3]. Düwel et al. [4] investigated Jet flames of ethanol with an emphasis on the size, velocity, and temperature The spatial progression of the scattered phase. Mikami et al. [5] counterflow research spray flames of n-heptane and n-octane poly- dispersed and came to the conclusion that changes in droplet size distribution is drastically altered affected spray burning behavior, leading to flames made up of droplets smaller than 50 μm that eventually turned into counterflow flames made by gas. The droplet-size distribution was also discovered to have an impact on the extinction limit. Poorhoseini et al. [6] impact of increasing the input the amount of air swirls in liquid fuel burners was explored. Discovered increase the swirl number reduced NO_x emissions and resulted in the combustion chamber's lower exhaust temperature. Zhou et al. [7, 8] studied effecting of increasing the liquid fuel burners' inlet air swirl number. Discovered that raising the swirl number would lower the combustion chamber's exhaust temperature and minimize nitrogen oxide (NO_x) emission. Finer mesh size turbulence was shown to improve evaporation, resulting in greater flame length. Zhou et al. [8] The impact of the swirl number on nitrogen oxide production generation was researched, and it was discovered that as the swirl number grew, the mean flame temperature gradually climbed. As the temperature of the exhaust outlet dropped, so did the amount of nitrogen oxide pollution. Bonatesta et al. [9] Studying the impact of the swirl number on exhaust soot concentration revealed that while the concentration of

exhaust soot emissions decreased as the swirl number increased to values greater than 2, the exhaust soot concentration gradually increased as the swirl number increased to values greater than 2. Patel and Shah. [10] carried out an experimental investigation to examine how varying fuel and air velocities affect a diffusion flame's appearance. Additionally, they looked at how different vane angles affected the swirling flow's influence on the length of the flame and found that swirling flow makes inverse diffusion flames (IDFs) shorter, broader, more reliable than (IDFs) without swirling flow. Patel and Shah. [11] The effects of enrichment of hydrogen on a swirling and non-swirling natural gas diffusion flame conditions were explored. They noticed that the flame was reduced when hydrogen was added duration and increased the temperature in both situations. while, the non-swirling flame had a far larger For a specific mass-based hydrogen addition quantity, the temperature rises above the whirling flame, which accelerated the non-swirling case's rate of NO_x pollutant formation. Khelil et al. [12] predicted the number of NO_x emissions from a high-whirling Numerical simulation of natural gas diffusion flame making use of the PDF combustion model and the RSM turbulence model. They discovered that a flame production in the center recirculation zone could be seen in the high-temperature zone. Additionally, this area had the highest rate of NO_x generation, whereas low temperatures had the lowest NO_x levels. The furnace's zone.

Khanafer and Aithal. [13] studied conducted a numerical analysis to look at how a natural gas diffusion flame's combustion pollutant, depending on the swirl number. They conducted this simulation using the commercial FIDAP program, and they deduced that raising the swirl number

considerably increased the fuel/air mixing rate and thus decreased Emissions from burning. They revealed that increasing the swirl number resulted in a 3–5 times reduction in (CO) and other unburned gases. Llbass et al. [14] analysed the impact of the swirl number (0-0.8) on the fuel mixtures' combustion properties in a gas-fired combustor. For more precise prediction in reactive modeling, using a coherent combustion model is crucial. Because it better captures the experimental data and is preferred for mixing fuels, the combustion model PDF/Mixture Fraction has been selected chosen as a result. The P1 radiation model and the k realizable turbulence model of turbulent flow were the other mathematical models used in this investigation. To validate the projections, methane was used as the baseline fuel in the models. It is demonstrated that forecasts and actual experimental data agree fairly well. Then, Using five distinct swirl numbers ranging from 0 to 0.8 at 0.2 intervals, the combustion properties of the hydrogen-containing fuel blends were modeled to determine the impact of the swirl number. Conclusion: Changes in the swirl number have a significant impact on the flame temperatures. Because the distribution of temperature in the combustor is significantly altered by the tangential velocity of the air stream. It is also shown that variations in the swirl number impact where the elevated NOX patches are located. Jones et al. [15] Axial-swirl combustion of kerosene spray has been studied using large eddy simulations (LES), with a particular focus on how evaporating droplets affect flame temperature and species concentrations. The dispersion (liquid) and gas phases are both treated using the LES-PDF approach. A Lagrangian formulation is used to describe the liquid phase, whereas an Eulerian method is used to describe the gas phase. With

a focus on the impact the influence of unresolved velocity and temperature fields on droplet evaporation rate, the prediction power of LES with sub-grid size models for spray dispersion and evaporation is evaluated. The findings The mean velocity fields of the fully connected LES formulation agree well. that were observed and those that were simulated. In the simulations, the overall behavior of the spray combustion, including droplet dispersion and evaporation, is quite effectively portrayed. It was discovered that the significant velocity changes seen in the shear layer significantly influence the rate of evaporation and, consequently, the temperature distributions. The current work also showed that LES might be used to investigate complicated flow characteristic of combustion chambers in gas turbine. Yilmaz. [16] In this modeling, the stable laminar flamelet combustion and the k. turbulence models that are feasible were utilized. According to the findings, the amount of hydrogen in the fuel has a significant impact on the flaming composition. The flame of natural gas diffusion was modeled by taking the swirl number into consideration. Khanafer and Aithal. [17] Studied NOx production is affected by temperature of the burner wall and swirl velocity. Using the commercial finite-element program FIDAP, velocity, temperature, pressure, and species concentrations were fluid-dynamic variables. estimated. The equations in the nonlinear system describing the generation of equilibrium products in fuel-air mixtures was solved using the Newton-Raphson technique. The major objective of this work was to create a quick and reliable computational method to comprehend how different design factors affect NOx production in gas-fired swirl burners. According to the findings, increasing swirl monotonically decreased CO and unburned petroleum. Up to 5 orders of

magnitude were reduced. The NO_x exit plane did not monotonically fall off as the swirl increased. NO_x readings initially rose as the swirl increased. And then got smaller. The method described in this research may be used to assess novel burner designs. And operational circumstances swiftly and effectively. Datta and Som. [18] To investigate the effects A computer model based on stochastic separated flow analysis of typical diffusion-controlled spray combustion of liquid fuel in a gas turbine combustor examines the effects of combustor pressure and input swirl on the combustion and emission characteristics within the combustor. was developed. It has been established that increasing the swirl number decreases NO_x emissions while improving pattern factor at all combustor pressures. However, although a rise in swirl number affects combustion efficiency at lower pressure, the pattern is exactly the opposite at higher pressure. The pattern factor improves as pressure increases, while combustion efficiency decreases and NO_x emissions rise. Rohani and Saqr. [19] are investigating at the influence of hydrogen on a tumultuous, unconfined, whirling methane/air flame's temperature and pollution emissions. The achievable k- combustion and turbulence models, as well as the constant laminar flamelet were used, respectively. Used probability density function. between 0 and 50 percent of the fuel volume flow rate, there is a large variation, is modeled for the proportion of hydrogen in the fuel stream. The outcomes reveal that the flare structure significantly changes as the volumetric hydrogen fraction in the fuel stream increases. Peak temperature rises as the extent of the highest temperature area shrinks considerably to a small region at the flame tip, increasing NO emission levels. The flame that contains 10% hydrogen is seen to marginally follow the typical pattern. Given

that the amount of hydrogen consumed is inadequate to modify the flame's combustion properties, this is believed to be the result of a change in flow field brought on by a change in fuel density.

Joung and Huh. [20] The fundamental swirling commercial methane-fueled gas turbine combustor and flames were investigated, and good experimental findings capturing the turbulence-chemistry link were discovered. Choi and Baek. [21] Radiation improved spray combustor performance by creating fast evaporation causes shorter droplet trajectories, which increases the size of the high-temperature area within the combustion chamber.

the first goal of this study is to examine the influence of swirl number on flame structure and emission parameters in a coaxial burner. In this regard, the emergence and emissions of the flame CO₂ and NO_x are evaluated using the swirled with a vane. Angle of 40°, 50°, and 60°. The impact of the radiation models and swirling flow on thermal efficiency and emission are examined.

2. Methodology

2.1. Liquid phase

In the gas phase (continuous phase), it has been suggested that the liquid phase (discrete droplets) is spherical. The trajectory of liquid-phase droplets at the beginning of solutions is determined by the model by combining the force balance using the Lagrangian technique. The following problem is solved for the liquid phase using the governing equations given in [22], which have been updated and amended after the gas phase has been computed and modified.

$$\frac{du_p}{dt} = f_D(u - u_p) + \frac{g_x(\rho_p - \rho)}{\rho_p} + \frac{\rho}{\rho_p} u_p \frac{\partial u}{\partial x_i} \quad (1)$$

$$f_D = \frac{18\mu}{\rho_p d_p^2} \frac{c_D R_e}{24} \quad (2)$$

$$R_e = \frac{d_p \rho |u_p - u|}{\mu} \quad (3)$$

Where the droplets velocity is u_p in (m/s), the drag force effect per unit particle mass is $f_D(u - u_p)$ in (m/s^2), the gravitational force effect on the droplet is ($\frac{g_x(\rho_p - \rho)}{\rho_p}$). The third term is an extra force on the right hand. created by the difference in pressure between the fluid. $\frac{du_p}{dt}$ Term denotes the evaporation rate of the particle. The gravity is g_x in (m/s^2), the droplet diameter is d_p , and the drag coefficient is C_D , and a_1 , a_2 , and a_3 can be defined as constants given by [23]. The heat balance for determining Heat transmission between the gaseous and liquid phases. Investigating the impact of the particles' drag force is one of the key factors. In order to character to rag force coefficient (CD), drag correlation Morse and Alexander [23] is used, presuming that the droplet has a spherical shape.

$$CD = a_1 + \frac{a_2}{R_e} + \frac{a_3}{R_e^2} \quad (4)$$

Where: a_1 , a_2 , and a_3 are constants. The differential in the concentration of vapor between the gas phase and the droplet surface influences the rate of vaporization. The term of the volumetric source denoted by S_h is can be expressed as follows:

$$S_h = \left[\frac{\bar{m}_p}{m_{p.o}} cp \Delta T_p + \frac{\Delta m_p}{m_{p.o}} (-h_{fg} + \int_{T_{ref}}^{T_p} C_{p,i} dt) \right] \dot{m}_{p.o} \quad (5)$$

Iterative techniques are employed to solve the two interconnected stages. After a particle

route has been estimated, the particle's mass, heat, and momentum gained or lost stream are calculated. The solid phase undergoes mass transfer from the liquid phase through then taken into account in the calculations for the gas phase. To calculate gas-phase S_m , the mass variations between the control volumes are used. These equations are used to compute it:

$$S_m = \frac{\Delta m_p \dot{m}_{p.o}}{m_{p.o}} \quad (6)$$

Where the particle mass change in each control volume is Δm_p , the initial mass flow rate of the particles is $\dot{m}_{p.o}$, and the mass flow rate of particles is m_p . The exchanging mass is then used as a source of mass in the gas-phase and species equation's continuity equation. The change in a particle's momentum across control volumes may be used to represent the momentum transfer between two phases using:

$$F_i = \sum \left(\frac{18\mu}{\rho_p d_p^2} \frac{c_D R_e}{24} (u - u_p) + \frac{g_x(\rho_p - \rho)}{\rho_p} + \frac{\rho}{\rho_p} u_p \frac{\partial u}{\partial x_i} \right) \dot{m}_p \Delta t \quad (7)$$

2.2. Gas-Phase

The equations for continuity, momentum, and energy conservation are the ones that control the Eulerian multiphase. Each phase is dealt with separately, and the gas phase is modeled as a continuum. The mass conservation equation is used, and it is applied to each phase of the system. The model simply takes into account the gas phase when a process starts, not the interaction of two phases. After the particle's trajectories are solved, the source term is obtained. Fluent Ansys resolves the gas phase by include the source term in the equation.

$$\frac{\partial}{\partial x_i} (\rho u_i) = S_m \quad (8)$$

Where in gas-phase, the air velocity is u_i in (m/s), The liquid phase's mass addition from the gas phase is S_m in ($kg/m^3 s$).

Momentum:

$$\rho u_i \frac{\partial u_i}{\partial x_i} = \frac{\partial}{\partial x_j} \left[\mu \left(\frac{\partial u_i}{\partial x_j} + \frac{\partial u_j}{\partial x_i} \right) - \frac{2}{3} \mu \left(\frac{\partial u_j}{\partial x_j} \right) \delta_{ij} \right] + \rho g_i - \frac{\partial p}{\partial x_i} + F_i \quad (9)$$

Where the momentum source term is F_i in (kg/m^2s^2), the gravity is g_i in (m/s^2), a molecular viscosity μ is in (kg/m^2s^2),

Energy:

$$\rho u_i \frac{\partial e}{\partial x_i} = -p \frac{\partial u_i}{\partial x_i} + \Phi v + \frac{\partial}{\partial x_i} \left(k \frac{\partial T}{\partial x_i} \right) + \frac{\partial}{\partial x_i} \left(\sum_{i=1}^n h_i J_i \right) + S_n \quad (10)$$

the static pressure is P in (pa), and the equation inclusion species diffusion and the exchange energy source between gas-phase and liquid-phase, the S_n volumetric heat source, estimates the heat transfer utilizing: where the internal energy is e in (J/kg), the Rayleigh dissipation function is Φv in (kg/S^2m), the thermal conductivity is K in (W/mk), the enthalpy of species i is h_i , the temperature of the air is T in (k). A species' diffusion flow is (J_j), and the volumetric heat source is S_n in (kg/S^2m). The equations for species conservation that forecast the local mass fraction of every species, gas-phase of liquid fuel and air, are:

$$\rho u_i \frac{\partial m_i}{\partial x_i} = -p \frac{\partial J_i}{\partial x_i} + S_m \quad (11)$$

$$J_i = -\rho D_{i,m} \frac{\partial m_i}{\partial x_i} \quad (12)$$

Where the local mass fraction of species i is m_i , and the diffusion coefficient for species i

the coefficient of the thermal expansion is β is the turbulent Prandtl number is Pr_t is

at default =0.85, the sours terms defined by used are S_k , S_ϵ and the reverse active prandtl are σ_ϵ , σ_k for ϵ, K respectively. Constants model at default value is: $C_{1\epsilon} = 1.44$, $C_{2\epsilon} = 1.92$, $C_m = 0.09$, $\sigma_k = 1$, $\sigma_\epsilon = 1.3$, $\sigma_{3\epsilon} = -0.33$.

in the mixture $D_{i,m}$.

2.3. Turbulence modelling

In practical and technological applications, there is a mathematical representation of turbulence called turbulent flow. The turbulence model was utilized to forecast the alteration of the turbulence using simple equations.

2.3.1. Standard k- ϵ modelling

The Standard model derivation ignores the effects of molecular viscosity and assumes that the flow is totally turbulent. It is only suitable for completely turbulent. According to their respective values for the turbulence dissipation rate ϵ , and the turbulent kinetic energy k :

$$\frac{\partial}{\partial t} (\rho k) + \frac{\partial}{\partial x_i} (\rho k u_i) = \frac{\partial}{\partial x_j} \left[\left(\mu + \frac{\mu_t}{\sigma_k} \right) \frac{\partial k}{\partial x_j} \right] + G_k + G_b - \rho \epsilon - Y_m + S_k \quad (13)$$

$$\frac{\partial}{\partial t} \rho \epsilon + \frac{\partial}{\partial x_i} (\rho \epsilon u_i) = \frac{\partial}{\partial x_j} \left[\left(\mu + \frac{\mu_t}{\sigma_\epsilon} \right) \frac{\partial \epsilon}{\partial x_j} \right] + C_{1\epsilon} \frac{\epsilon}{k} (G_k + C_{3\epsilon} G_b) - C_{2\epsilon} \rho \frac{\epsilon^2}{k} + S_\epsilon \quad (14)$$

$$\mu_t = \rho C_m \frac{k^2}{\epsilon}, \quad G_k =$$

$$-\rho u'_i u'_j \frac{\partial u_j}{\partial x_i}, \quad G_b = \beta g_i \frac{\mu_t \partial T}{Pr_t \partial x_j}$$

Where: The Turbulent viscosity is μ_t , the effect of buoyancy is G_b the Rate of dissemination is Y_m , turbulent kinetic energy generation is G_k , and the Turbulent velocity is u' ,

2.4. Combustion model

The probability density function (pdf) was used in this study to assess a few combustion parameters. A clipped Gaussian and a beta function are two different forms of probability density functions that can be derived from the

mixture fraction to show the amounts of the conserved scalar that are impacted by the turbulence fluctuation. A beta function is frequently employed in the current study because of its simplicity and affordability. Mathematical identification of the beta function:

$$p(f) = \frac{f^{\Psi-1}(1-f)^{B-1}}{\int_0^1 f^{\Psi-1}(1-f)^{B-1} df} \quad (15)$$

$$f = \frac{z_i - z_{i,ox}}{z_{i,fuel} - z_{i,ox}} \quad (16)$$

Where the coefficients Ψ and B are representing the explicit functions of the mass average mixture fraction (\bar{f}) as well as the concentration fluctuation (g), described by

$$\Psi = \tilde{f} \left[\frac{\tilde{f}(1-\tilde{f})}{g} - 1 \right] \quad (17)$$

$$B = (1-\tilde{f})\Psi \quad (18)$$

When the \tilde{f} and g are determined from the Finite Difference solutions at each grid point, the species concentration mean values, product temperature, density, and enthalpy are determined by weighting these quantities with pre-assumed Probability Density Functions of the mixture fraction, $\check{p}(f)$ might be adequately specified. The Favre-averaging quantity \tilde{Q} can be determined from the quantities of each $y_i(f)$, $H_i(f)$, $T(f)$, and $\rho(f)$ are representing the instantaneous of the mixture fraction (f).

$$\tilde{Q} = \int_0^1 \check{p}(f) Q(f) df \quad (19)$$

After determining Ψ and p from the defined values of \tilde{f} and g using both (17) and (18) equations, additionally, Beta PDF depends only on the Mixture Fraction. Appropriate number for example $N=100$ of separate amounts of $Y_i(f)$, $T(f)$, etc., were accounted from the state equations for mixture fraction in the domain (0-1) and stocked in tabular formulating.

2.5. Radiation

2.5.1. Discrete ordinate method

The radiative transfer equation (RTE) for a finite number of discrete solid angles, each with its own vector direction, is solved using the discrete ordinates radiation model. Stuck in Cartesian space, you select the degree of angular discretization fineness. Similar to how you choose the fineness of the angular discretization. The DTRM has a certain number of rays. The DO model, unlike the DTRM, uses no ray tracing technology.

Instead, the DO model turns Equation (RTE) into a radiation intensity transfer equation in spatial dimensions (x, y, z). The DO model may answer any number of transport equations. Directions the method of solution is the same as for the energy and fluid flow equations. In ANSYS Fluent,

The DO model comes in two varieties: (energy) connected and uncoupled. The finite-volume approach is used in the implementation that is not linked, which is inherently sequential. (24), (25), and its extension to unstructured meshes [26] as a conservative form of the DO model. One by one, Energy and radiation intensity equations have been solved. In the uncoupled case, assuming constant values for other variables. At each cell, the discrete energy and intensity equations are determined concurrently in the linked ordinates method (or COMET) [27], given that spatial neighbors are known. The linked technique has the advantage of speeding applications that need thick optical films. heightened scattering indices and/or nesses when using the sequential technique, such applications significantly impede convergence.

The Discrete ordinate (DO) Model Equations

The radiative transfer equation (RTE) in the direction (s) is regarded as a field equation by the DO model. is written as.

$$\nabla \cdot (I(\vec{r}, \vec{s})\vec{s}) + (\alpha + \sigma_s)I(\vec{r}, \vec{s}) = \alpha n^2 \frac{2\sigma T^4}{\pi} + \frac{\sigma_s}{4\pi} \int_0^{4\pi} I(\vec{r}, \vec{s}) \Phi(\vec{s}, \vec{s}) d\Omega \quad (20)$$

ANSYS Fluent can also model A gray-band model is used to simulate non-gray radiation.

The level of spectral intensity RTE λ (r \vec{r} , s \vec{s}) can be written

$$\nabla \cdot (I_\lambda(\vec{r}, \vec{s})\vec{s}) + (\alpha_\lambda + \sigma_s)I_\lambda(\vec{r}, \vec{s}) = \alpha_\lambda n^2 I_{b\lambda} + \frac{\sigma_s}{4\pi} \int_0^{4\pi} I_\lambda(\vec{r}, \vec{s}) \Phi(\vec{s}, \vec{s}) d\Omega \quad (21)$$

Here λ is the wavelength, α_λ is the coefficient of spectral absorption, and $I_{b\lambda}$ is the Planck function's black body intensity. The scattering coefficient, scattering phase function, and refractive index n are considered to be wavelength independent. The non-gray DO implementation splits the light spectrum into N. wavelength bands, which do not have to be continuous or of equal length. You supply the wavelength intervals, which correspond to vacuum values (n = 1). The RTE is integrated across each wavelength interval, yielding quantity transfer equations.

[I] λ $\Delta \lambda$, radiant energy stored within the wavelength band $\Delta \lambda$.

Energy Coupling and the DO Model

The connection of the concentration of the intensity of the convergence of the finite volume scheme for radiative heat transfer is accelerated by energy and radiation at a cell (also known as COMET). [28] for applications involving optical thicknesses, this approach leads in a significant improvement in convergence. This is most commonly seen in glass melting applications. with values greater

than 10. This feature is beneficial. When there is substantial dispersion, the directional radiation intensities are strongly coupled. The DO/Energy Coupling option in ANSYS Fluent is used to build this Discrete ordinate model. In the Radiation Model dialog box, select the DO model option. For the discrete energy equations below are some examples of connected methods.

When The energy equation is solved across a control volume I. the equation for discrete energy is obtained:

$$\sum_{j=1}^N \mu_{ij}^T T_j - \beta_i^T T_i = \alpha_i^T \sum_{k=1}^l I_i^k \omega_k - S_i^T + S_i^h \quad (22)$$

$$\alpha_i^T = k \Delta v_i$$

$$\beta_i^T = 16k\sigma T_i^{*3} \Delta v_i$$

$$S_i^T = 12k\sigma T_i^{*4} \Delta v_i$$

$\Delta v = control\ volume$

The coefficient μ_{ij}^T and the source term S_i^h are caused by Convection and diffusion are discretized. factors, in addition to the non-radiative source terms. the energy discretization equation, Equation (22) yields (23).

2.5.2. The P-1 Radiation Modelling

The P-1 radiation model is a condensed variant of the P-N model in which I is extended into an orthogonal series of spherical harmonics. [29], (30). The equations utilized in the P-1 model are detailed in this section. See Using the Radiation Models for details on how to set up the model. The P-1 radiation model is the most basic version of the P-N model. If just four terms in the series are used to approximate gray radiation, the radiation flow is given by the following equation:

$$q_r = \frac{1}{3(a + \sigma_s) - C\sigma_s} \nabla G \quad (23)$$

Where the absorption coefficient is α , the scattering coefficient is σ_s , the incoming radiation is G , and the linear-anisotropic phase function coefficient is C . Following the parameter's introduction.

$$\Gamma = \frac{1}{(3(a + \sigma_s) - C\sigma_s)} \quad (24)$$

Equation (23) simplifies to

$$q_r = -\Gamma \nabla G \quad (25)$$

The transport formula for G is

$$\nabla \cdot (\Gamma \nabla G) - aG + 4an^2\sigma T^4 = S_G \quad (26)$$

Where σ is the Stefan-Boltzmann constant, n is the medium's refractive index, and S_G is a radiation source that is defined by the user. The equation is solved by ANSYS Fluent to produce the incident radiation. When the P-1 model is in operation. Formula Combination (17) and Equation (18) yields the following equation:

$$-\nabla \cdot q_r = aG - 4an^2\sigma T^4 \quad (27)$$

The expression for $-\nabla \cdot q_r$ may be used to directly account for heat sources in the energy equation (or sinks) induced by radiation. To mimic non-gray radiation with a gray-band model, Equation (18) is modified as follows:

$$\nabla \cdot (\Gamma_\lambda \nabla G_\lambda) - a_\lambda G_\lambda + 4a_\lambda n^2 \sigma T^4 = S_{g\lambda} \quad (28)$$

Where n is the medium's refractive index, a_λ is the spectral absorption coefficient, and G_λ is the spectrum of incident radiation, $S_{g\lambda}$ is a user-defined source term. Γ_λ is defined as:

$$\Gamma_\lambda = \frac{1}{(3(a_\lambda + \sigma_{s\lambda}) - C\sigma_{s\lambda})} \quad (29)$$

Where C is the coefficient of the anisotropic linear phase function and $(\sigma_{s\lambda})$ is a spectrum scattering coefficient. Black body spectral emission ($G_{b\lambda}$) between wavelength λ_1 and λ_2 .

$$G_{b\lambda} = 4[F(0 \rightarrow n\lambda_2 T) - F(0 \rightarrow n\lambda_1 T)]\sigma T^4 \quad (30)$$

Where $F(0 \rightarrow n\lambda)$ is the portion of radiant energy that a black body emits in the wavelength range. The wavelength boundaries of the band are λ_1 and λ_2 , and it ranges from 0 to λ at temperature T in a medium with refractive index n . The following formula is used to calculate the spectral radiative flux: $2T$

$$q_\lambda = -\Gamma \nabla G_\lambda \quad (31)$$

The energy equation's radiation source term is expressed as

$$-\nabla q_r = \sum_{AllBands} -\nabla q_{r,\lambda} = \sum_{allBands} a_\lambda (G_\lambda - n^2 G_{b\lambda}) \quad (32)$$

3. Numerical method, operating parameters and boundary conditions

The Ansys Fluent 15.0 is employed to solve all of the governing equations. Three-dimensional geometry in the Cartesian coordinate system has been solved using the pressure-based stable solver. The SIMPLE algorithm was used to carry out the coupling between pressure and velocity. Power law is used to discretize the variables in momentum and mixture fraction equations. Second order up winding the solution, an unstructured approach, whereas the energy equation is discretized using this scheme. Simulations in the discrete phase and continuous gas phase have been carried out. 300 continuous phase iterations are taken into account for each discrete phase iteration when iterating. Twenty in the simulation the test conditions of kerosene/air spray are mentioned in table (1).

Table (1) Numerical test conditions [33]

Fuel conditions		Units
Injector inlet and ambient temperature	300	k
Injector diameter	0.25	mm
Air initial velocity	8.66	m/s
Fuel initial velocity	28	m/s
Injector's flow rate	3.6×10^{-4}	Kg s^{-1}
Mass flow rate of air	0.04	kg s^{-1}
Injection pressure	6	bar

Just before the combustor zone, a swirler is installed in the primary air stream (Figure 1). In this study, three distinct swirler vane angles of 40° , 50° , and 60° were used to examine the impact of degree of swirl on key combustion characteristics. The relation [33] is used to compute the swirl number.

$$SN = \frac{2}{3} \frac{(D_s^3 - D_h^3)}{(D_s^2 - D_h^2)(D_s - D_h)} \tan \theta \quad (33)$$

Where, as shown in Figure 1, D_s is the outside diameter of the swirler, D_h is its hub diameter, and θ is the vane angle. The turbulence intensity is set at 4% for both the primary and secondary intake, and the the scale of length is 0.007 m. Based on the maximum mixing length of the combustor duct [33], the length scale was selected. The outlet boundary's The pressure outlet boundary condition was chosen. Stainless steel is the only material that has been specified for the walls. To allow for to account for heat loss from the system to the atmosphere, a mixed (convection and radiation) boundary condition has been devised. on the assumption that the walls are non-slip. A value determined for the coefficient of Heat transfer between the outside wall and the surrounding environment.

had been supplied in addition to the external and interior emissivity of the material used to form the wall surface. The environment temperature is set at 300 K, and the wall's thickness is assumed to be 5 mm. The fuel injector wall, however, is thought to be adiabatic. All of the walls are designated as reflecting walls for DPM calculations. Figure 2. Depicts the two-dimensional structural grid's computational domain. The region adaption strategy is used in this research. It is appropriate for a specific solution domain region. A two-dimensional inside improvement of the quadrilateral is examined. The standard case, which delivers the best numerical simulation to the experimental data when compared without mesh, is reached after two cycles of adaption. The number of mesh has affected numerical results, as seen in figure 3. As a result, three adoptions are employed. Using initial adaption (20800,42052,21253), some numerical results were obtained. As a second adaption, a higher mesh density (83200,167304,84105) is used in the next step. The outcome in this example differs from the initial adaption. The final adaption (83200,167304,84105) is then achieved by using a higher cell density. All numerical values obtained using the third adaption are comparable to those obtained using the second adaption. The numerous Mesh generators generate meshes with varying cell volumes. increase quickly as they get farther away from boundaries. While this naturally prevents a mesh from becoming too dense, it can become problematic If the mesh is too coarse to halt the flow. Region adaptation can be used to refine the mesh if in some areas of a solution domain, a finer mesh is necessary. For places that demand high resolution, region adaption is particularly crucial. Two-dimension is used in this work. The computational domain employed in two

situations is depicted in Figure (2). The results from the three levels of grid resolution are various in the three levels: coarse, medium, and fine. The best results show in the third level (fine grid).

Figure 1 shows a model combustor schematic, as well as swirlers with variable vane angles.

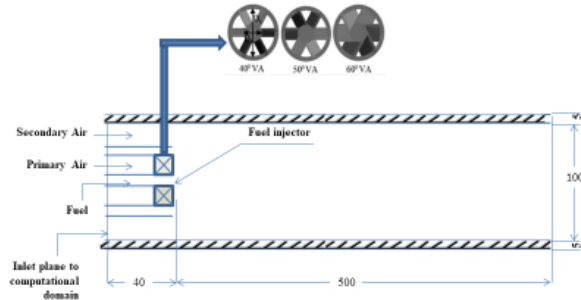
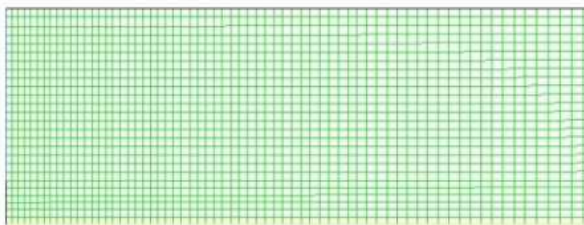
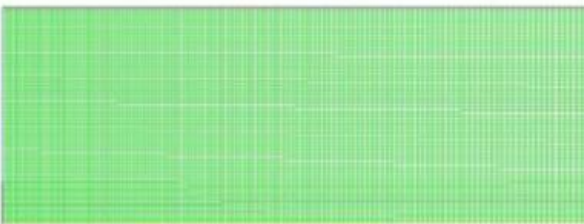


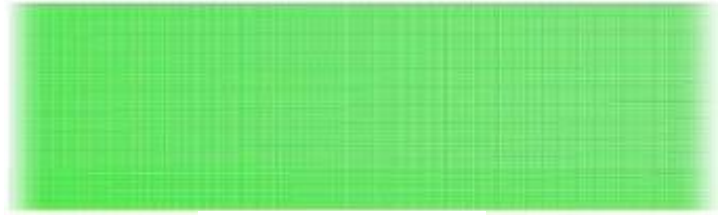
Figure 2. The computational domain. Numerical values obtained using the third adaption are comparable to those obtained using the second adaption



a. Coarse mesh



B-Medium mesh

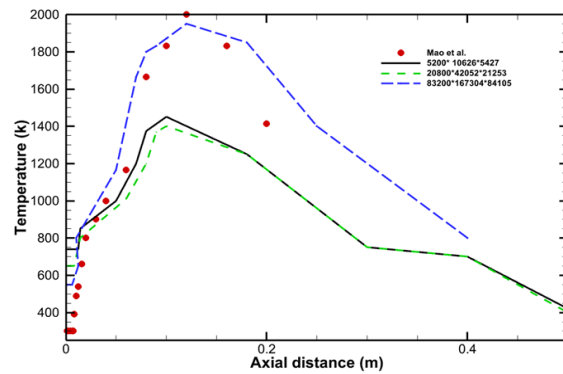


C. Refine mesh

Table (2). The grid specification

Details	Coarse mesh	Medium mesh	Refine mesh
CELL	5200	20800	83200
Faces	10626	42052	167304
Nodes	5427	21253	84105

Figure 3. Comparison between the adaption effects of prediction gas temperature with experimental data.



4. Results and discussion

The numerical model's validation has been carried out, and our goal is to determine the turbulence-chemical interaction using the significantly reduced chemistry used in the current model by comparing the agreement between the present prediction and the

experimental data. This initial round of validation does not cover the interactions between the phases of the gas and the drop. though, because the fuel is thought of as pre-vaporized kerosene Figure (4) shows the midline temperature change in a turbulent kerosene vapor-air diffusion flame based on measurements, current predictions, and the injection conditions of spray droplets, taken from Ghose et al. [33]

1. shows the comparison of gas temperature with swirl angle (40) between radiation models (P1, discrete ordinate, Roseland, surface to surface) and Ghose et al [33]. where the temperature in the experiment is 2050 (k) around 0.18(m). The numerical solution of spray combustion using the DO model gives an approximate trend with the measured results.

2. Figure (5) shows the comparison of gas temperature with swirl angle (50) between radiation models (P1, discrete ordinate, Roseland, surface to surface) and Ghose et al. [33], where the temperature in the experiment is 2100 (k) about 0.11 (m). The numerical solution of spray combustion using the p1 model gives an approximate trend with the measured results.

3. Figure (6) shows the comparison of gas temperature with swirl angle (60) between radiation models (P1, discrete ordinate, Roseland, surface to surface) and Ghose et al. [33], where the temperature in the experiment is 1400 (k) around of 0.02 meter. The numerical solution of spray combustion using the p1 model gives an approximate trend with the measured results.

4. The difference between case 1 and the numerical simulation was reported as 0.9% of the DO results, 2.0% of the p1, 2.0% of the

surface-to-surface, and 2.7% of the Roseland model.

5. The difference between case 2 and the numerical simulation was reported as 1.9% of the p1 results, 1.10% of the DO, 1.11% of the surface-to-surface, and 2.2% of the Roseland model.

6. The difference between case 3 and the numerical simulation was reported as 0.9% of the DO results, 1.0% of p1, 0.9% of surface-to-surface, and 7% of the Roseland model.

Figure 4. Comparison between calculated gas temperatures predicted around swirl angle (40) by p1, Discrete ordinate, Roseland, and Surface -to -Surface radiation model and Ghose et al[33]

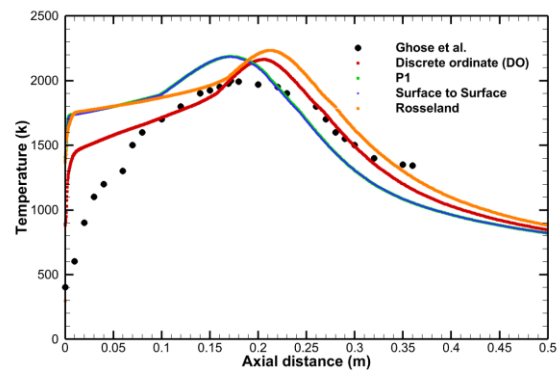


Figure 5. Comparison between calculated gas temperatures predicted around swirl angle (50) by p1, Discrete ordinate, Roseland, and Surface -to -Surface radiation model and Ghose et al[33]

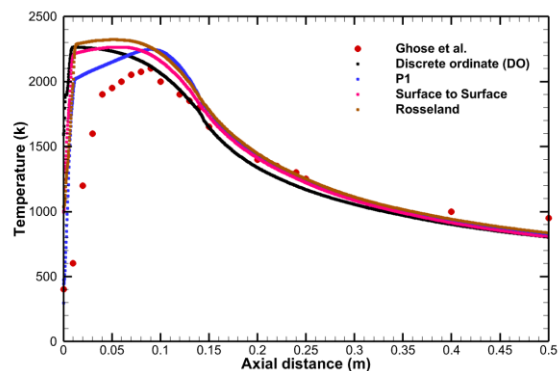
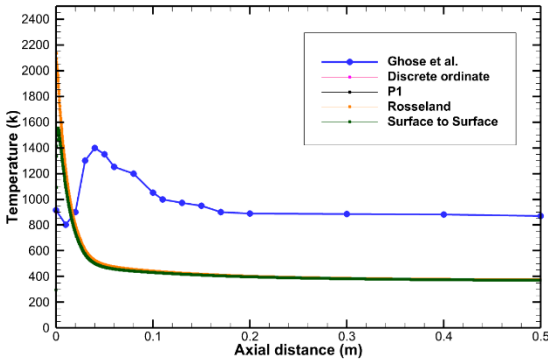


Figure 6. Comparison between calculated gas temperatures predicted around swirl angle (60) by p1, Discrete ordinate, Roseland, and Surface -to -Surface radiation model and Ghose et al [33]



The exhaust gas temperature pattern should thus be quite adequately indicated by the measuring of temperature in a single radial direction. However, the anticipated temperatures originating from the same horizontal plane were used to conduct the comparison. As they were utilized in the experiment. Along the whole radius of the combustor, it is shown that the expected and observed exhaust gas temperatures are quite close. the flame's temperature and the pace at which energy is transferred from the hot gas both affect how hot the exhaust gas is distributed. A good correlation between projected and measured exhaust gas temperatures strongly suggests that the combustion chamber's chemical and transport processes may be satisfactorily predicted. The effects of various the impact of swirl levels on the temperature distribution in the combustor has been quantitatively calculated. examined in this work. As shown in Table 3, the computational work was done using three distinct swirler vane angles in the primary air flow: 40° 50° and 60°. The table also includes the associated swirl numbers [3]. The next sections contain the numerical results for the

three separate scenarios. Except for close to the swirler and the inlet plane of the combustor, it has been noted that the axial symmetry is adequate in the findings has not been attained. As a result, the findings are primarily shown in a vertical plane that passes through the axis of the combustor.

Table 3. Swirler vane angles are used in simulations.

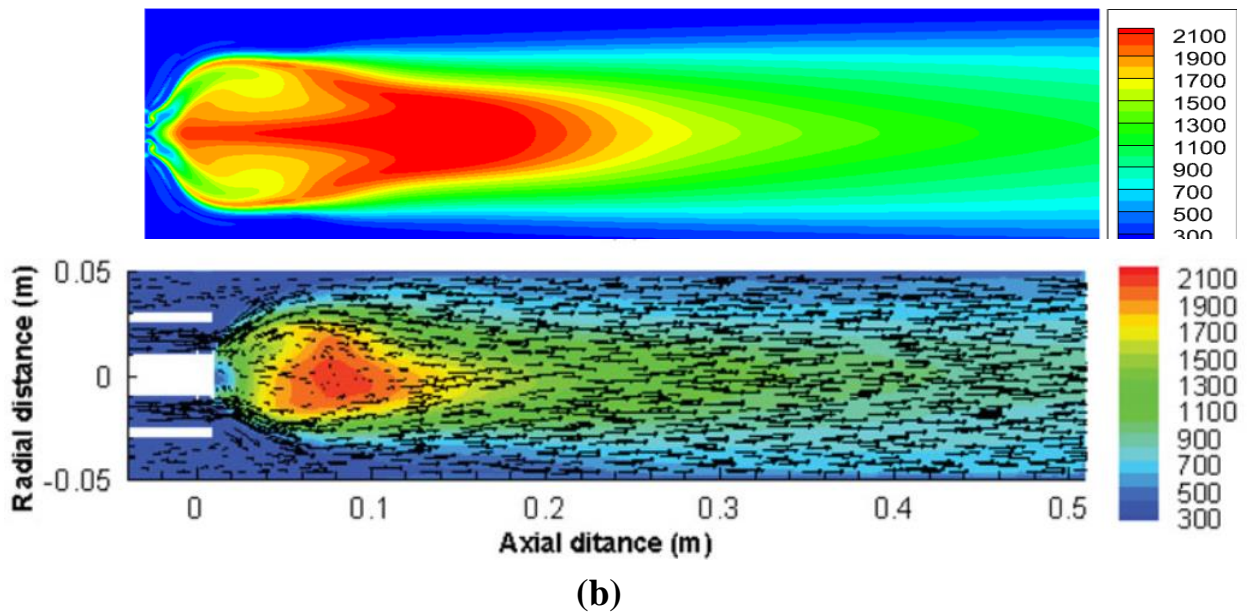
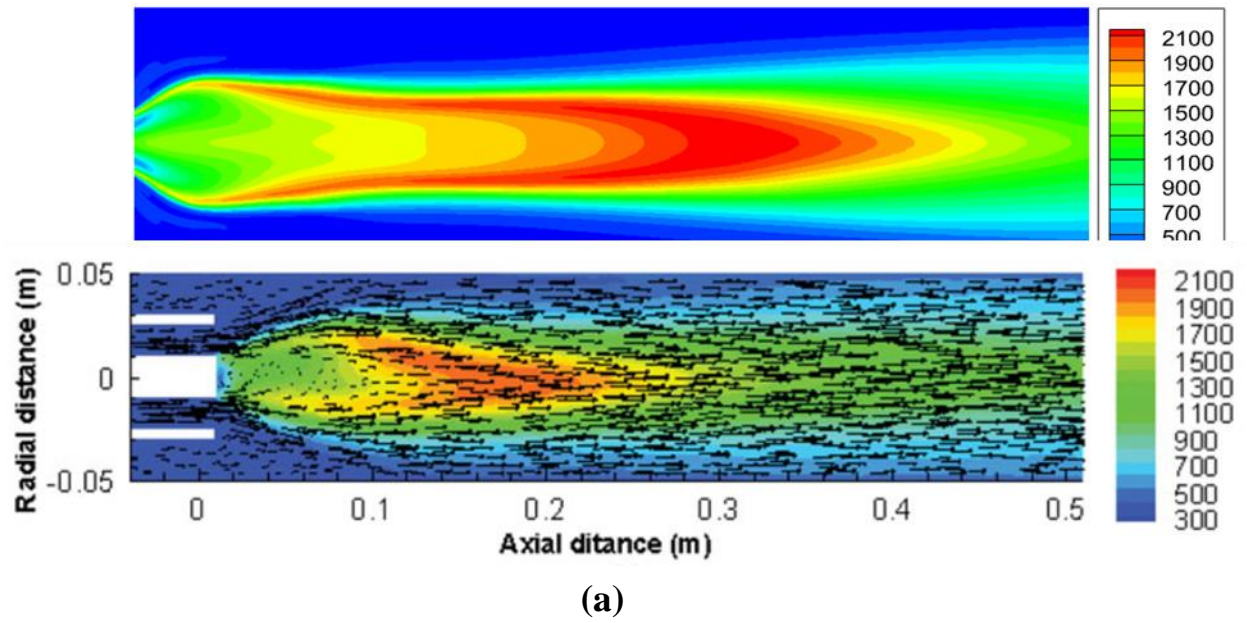
case	Vane angle(°)	Swirl number
A	40	1.038
B	50	1.474
C	60	2.142

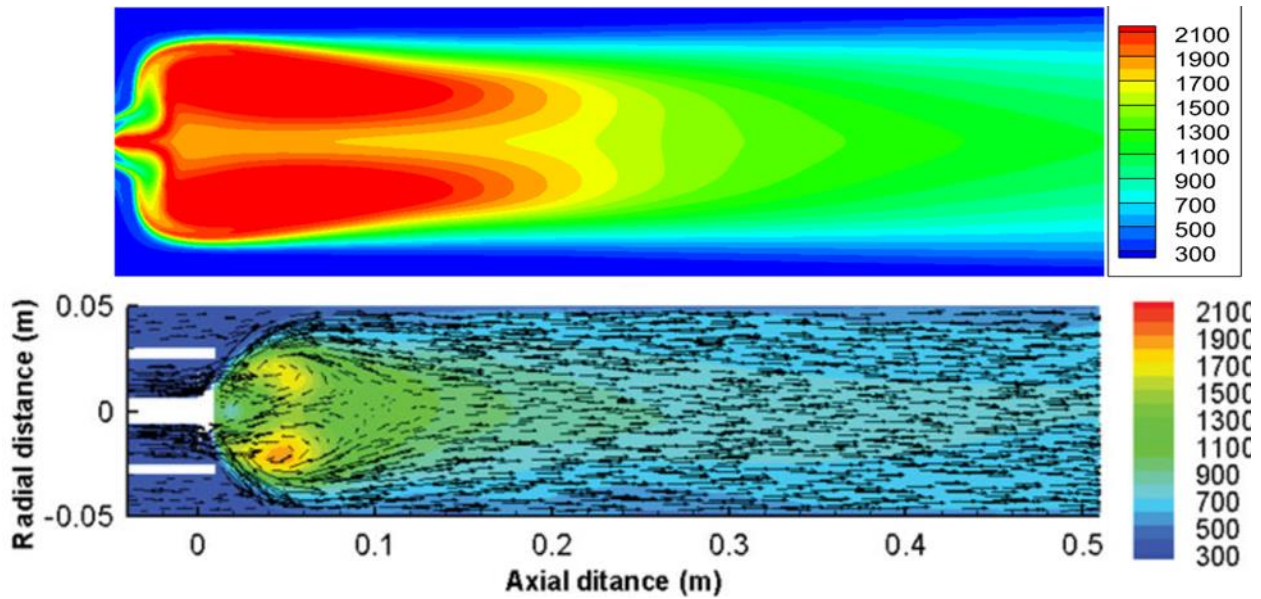
The numerical model's validation

Velocity and temperature distributions

Figures 7(a)–(c) depict temperature contours over the combustor axis in vertical planes, as well as the corresponding velocity vectors, for the three swirl scenarios (Table 3). The region of high temperatures that forms in the combustor can be used to represent the flame region. The statistics show that the flame in the combustion chamber is relatively long for the primary air case with a modest swirl (Case A), however, as the swirl strength increases, the flame gets smaller and smaller. The primary flow enters tangentially surrounding the axis of the combustor, and a central toroidal recirculation zone is formed. In Case A,

Figure 7. Temperature change shows vectors of velocity with different swirler vane angles superimposed on the center vertical combustor plane.: (a) 40 ; (b) 50 ; and (c) 60 .





(c)

Due to the low swirl number at flow entry, the recirculation zone's strength is quite low. The fuel that was injected evaporates, combines with air, and travels axially ahead to burn around the center axis under the influence of flow. Because of this, the zone with the maximum temperature is the flame grows downwind of the central on-axis vortex and is on-axis. In this situation.

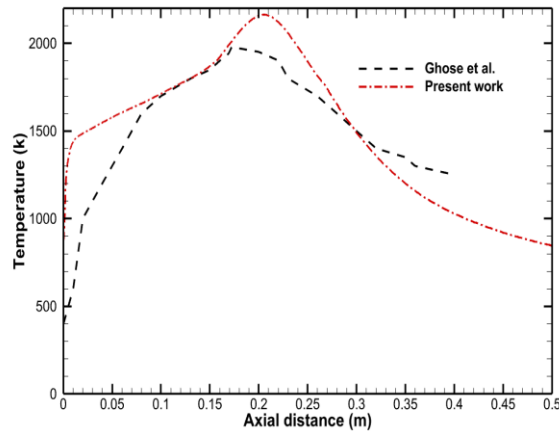
1. The peak temperature is estimated to be 1989 K and is situated 0.17 m from the combustor's inlet plane.

2. The central recirculation gets stronger after it reaches 1.475 when the inlet swirl number (Case B). The fuel-air combination is concentrated closer to the inlet than before thanks to the powerful recirculating bubble. The maximum temperature contours, which reflect the flame zone, continue to be on the axis but migrate near to the entrance (Figure 7(b)).

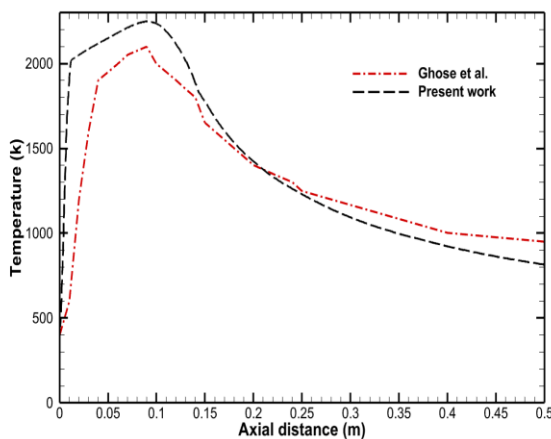
3. The maximum temperature (2060 K. Due to more vigorous burning than at 0.07 m from the combustor inlet), the prior instance.

4. The reverse flow is considered in Case C for the maximum swirl number. Recirculation grows to be so strong that it takes gas from an upstream source. area and quickly transports it upstream (see Figure 7(c)). The flame is split by the powerful reverse flow. Off-axis forces cause it to shift. Consequently, the flame takes on an annular figure and spreads throughout the radial motion. The recirculation bubble's powerful vertical patterns provided considerable flow turbulence. The peak temperature drops to 1863 K as a result of the turbulence, which occurs at 0.05 meters away from the combustor inlet plane and 0.02 meters below the combustor axis. The structure of flame structure is illustrated by the temperature dispersion along the combustor centerline.

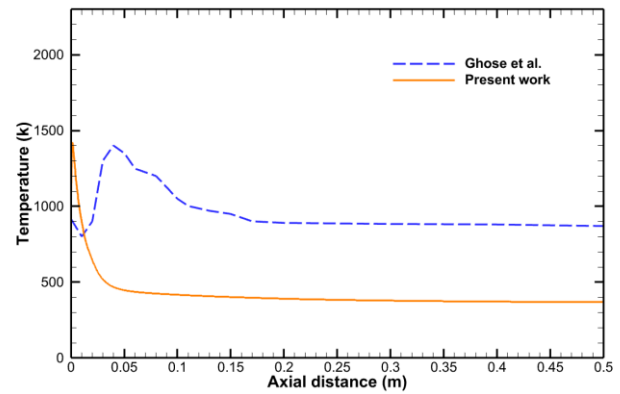
Figure 8 (a-d). Comparison between Ghose et al and Present work for Temperature fluctuation: velocities at various swirler vane angles are superimposed at the middle of the vertical combustion chamber. (1) 40° (Case A); (2) 50° (Case B); (3) 60° (Case C).



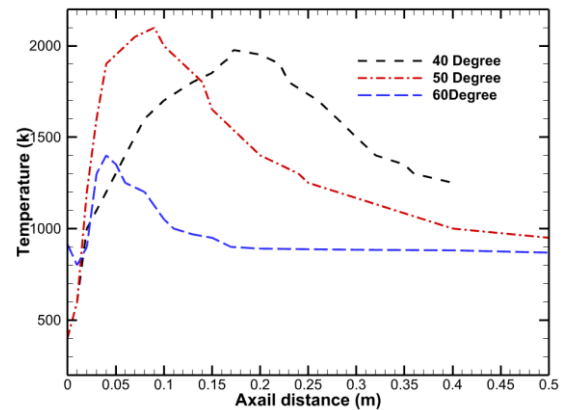
(a)



(b)



(c)



(d)

The variations in temperature along the center x-axis at various degrees of swirl are seen in

Figure 8. The centerline temperature was determined in Case A at 0.173 m from the combustor intake. first rises until reaching its highest value of 1977 K. There is a drop in temperature after attaining the highest value, along the axial direction.

The centerline temperature distribution for Case B similarly follows the same pattern. However, in this instance, the higher temperature is reached a little bit higher and at a somewhat upstream location (0.066 m from the combustor inlet plane) (2050 K). The shorter flame length in Case B compared to

Case A is thought to be the cause of the shift in distribution.

At Case C, there are some differences in the centerline temperature distribution. The temperature on the injector at the combustor entrance plane is around 915 K in this instance, which is greater than the comparable values in the preceding two situations.

The temperature initially decreases for a short distance before rising to its greatest amount at 0.044 m the combustor. This case's high centerline temperature of 1467 K is significantly reduced than the same value in the two cases with lower swirl numbers before it. The radiation from the short, nearby flame, which is the likely cause of the high swirl scenario and the temperature on the injector surface. As a result, in this instance, the injector is far more affected by radiative heating. Furthermore, As the flame goes the higher temperature on the centerline is lower than in the other two situations to an off-axis site with considerable swirl.

Species mass fraction distribution along the axis

Species mass fraction distribution along x-axis the distribution of several important species along the center region is depicted in Figure (9,10 and 11). As shown in Table 3, the combustor's axis for various swirl numbers. The proportion of plotting species (indicated on the secondary axis) identifies the reaction in the pictures. Zone on the centerline of the combustor.

The fuel (C₁₂H₂₃) vapor in the lowest swirl case According to Figure 9 (a - f), the mass fraction at the injector is 0.845. At about from the injector plane by 0.13 m the fuel vapor. the concentration quickly drops to less than 0.001. At this range,

2. The mass fraction of O₂ is almost 0.003, and it climbs downstream from here. Where the CO₂ also peaks in concentration.

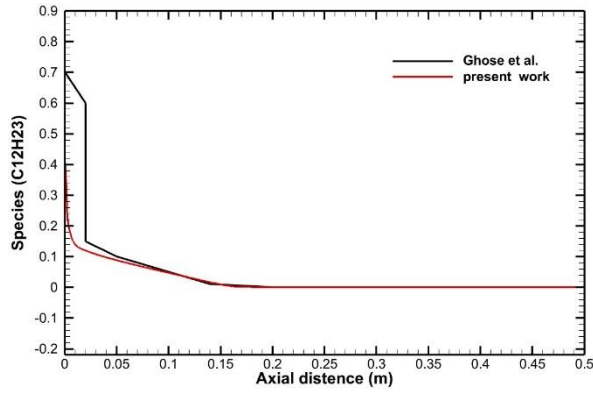
3. On the central axis, the greatest H₂O mass fraction occurs just before the CO₂ peak is reached. The flame's length decreases as the swirl number rises to 1.474 . Keeping close to the centerline Figure 10 (a - f).

The peak mass fraction of co₂ happens at in this instance, 0.086 m. higher co₂ mass fraction shifts near with relation to the injector as well. Plane (0.043 m),

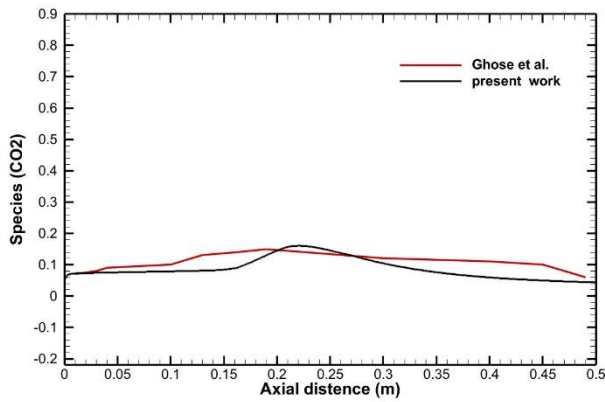
whereas the swirl number rises to 2.142. (Case C). Further, in the centerline higher co₂ mass fraction value in this instance (8×10^{-4}) is lower than that in the prior two instances (2×10^{-3}) this is explained by the fact that the off-axis flame with the greatest number of swirl cases.

Gaseous mixture is returned from a place upstream to one downstream by the powerful central recirculation. As a result, figure 11 (a - f) had a significantly lower concentration of fuel vapor nearby than the other two cases. In the highest swirl instance, the centerline oxygen concentration likewise rises relatively early. It validates the cause of the earlier noticed early soot oxidation and shows the impact of swirl on the air and fuel mixing. Secondary air is used to dilute the product stream outside of the flame zone has the effect of gradually raising the oxygen content while lowering CO₂ and H₂O concentrations are examples of additional product species. Well before the combustor the CO₂ concentration becomes zero. output, suggesting that the process has finished

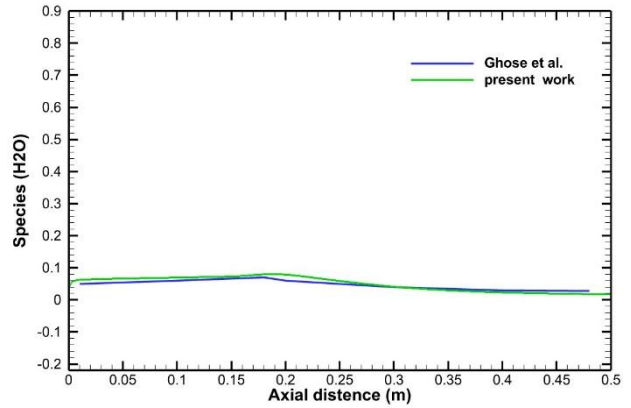
Figure 9 (a - f). Comparison between Ghose et al and Present work for at a swirler vane angle of, 40°the species mass fraction distribution along the axis is shown.



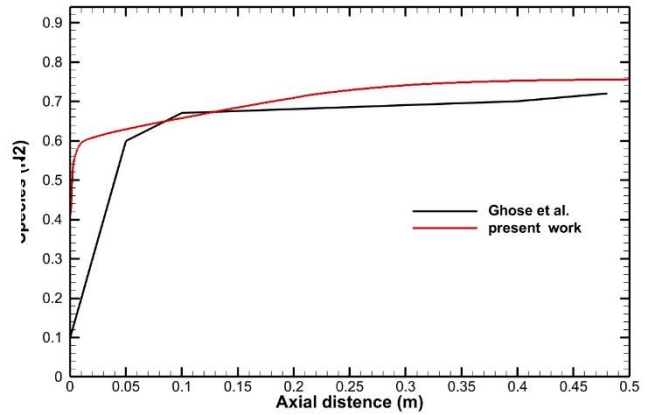
(a)



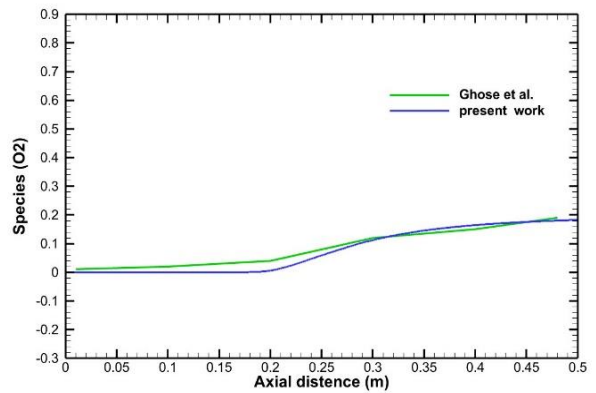
(b)



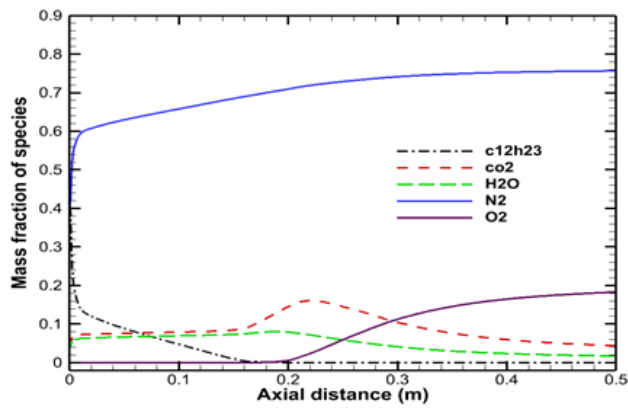
(c)



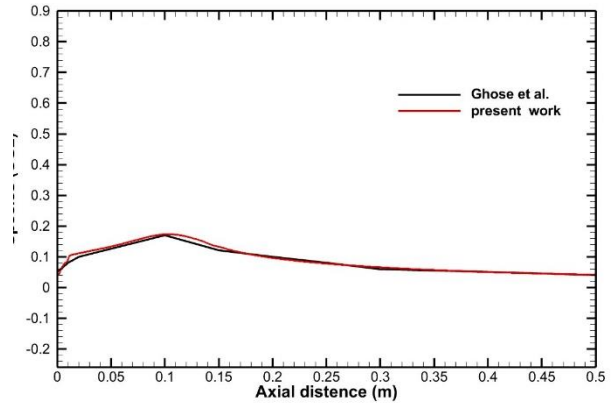
(d)



(e)

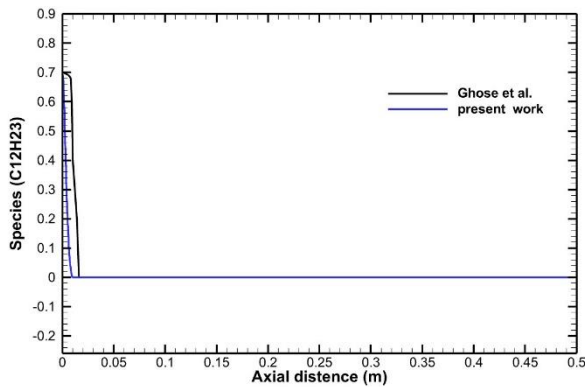


(f)

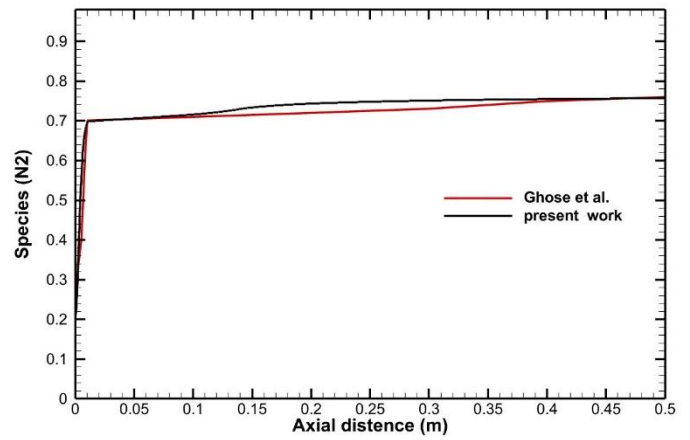


(b)

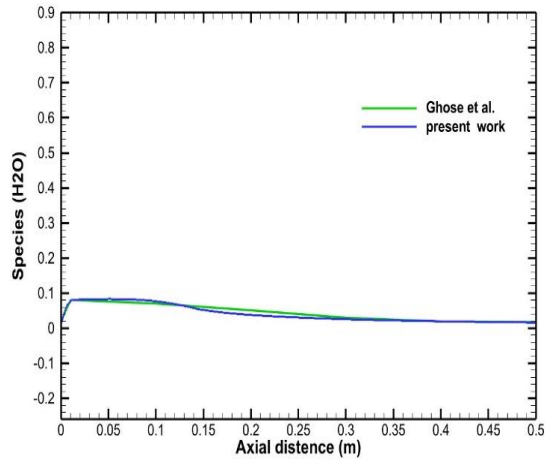
Figure 10(a - f). Comparison between Ghose et al and Present work for the distribution of species mass fraction along the axis is depicted with a swirler vane angle of 50.



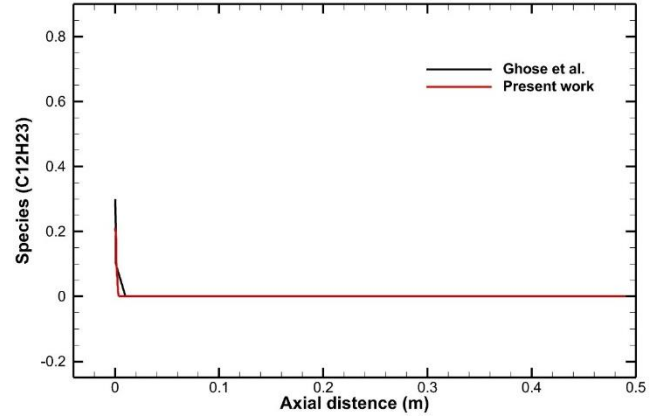
(a)



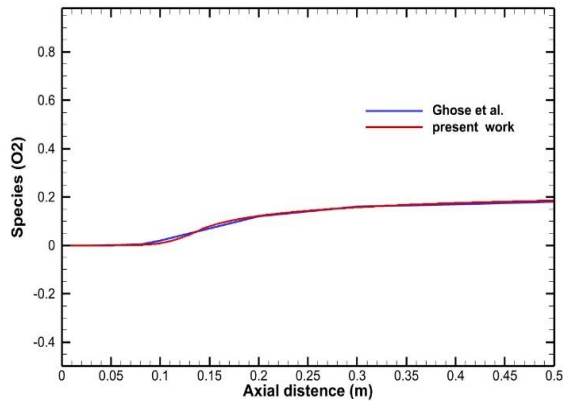
(c)



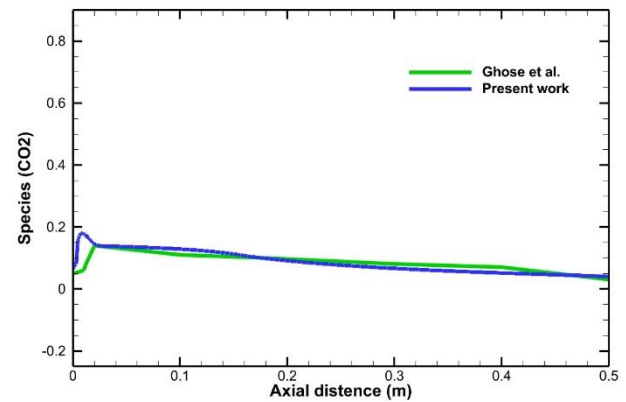
(d)



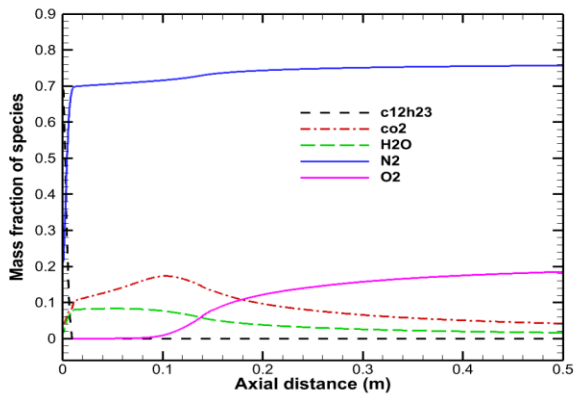
(a)



(e)



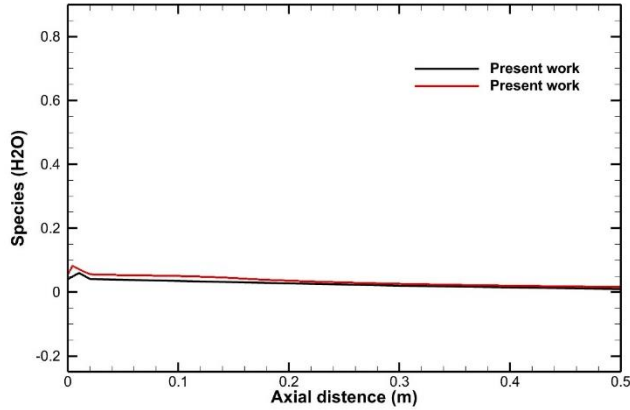
(b)



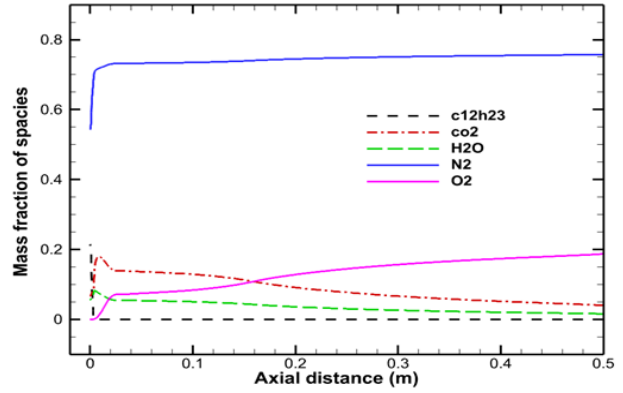
(f)

Figure 11(a-f). Comparison between Ghose et al and Present work for at a swirler vane angle of 60° , the distribution of species mass fractions along the axis is depicted.

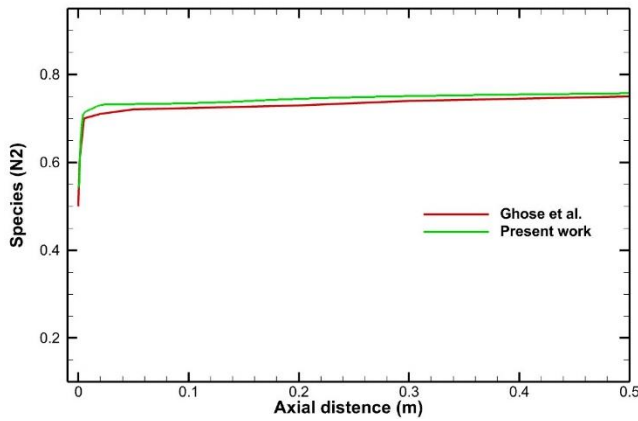
Effect of swirl angle on radiation models and spray flame



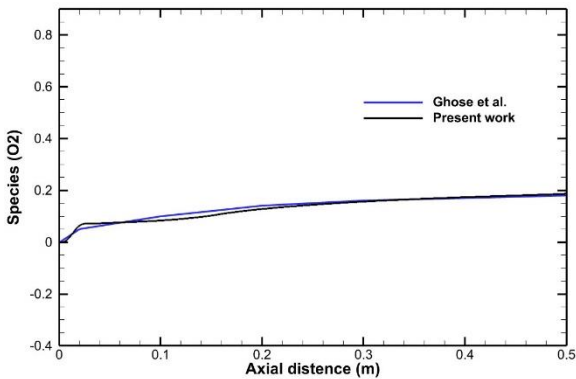
(c)



(f)



(d)



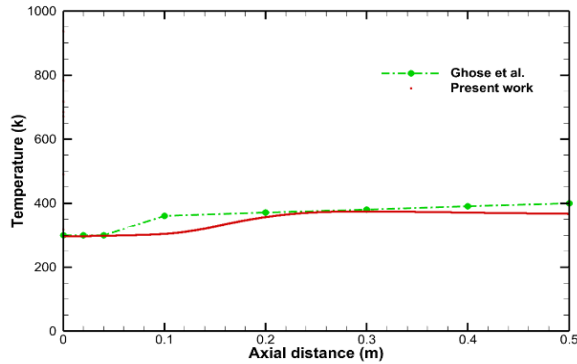
(e)

The temperature on the swirler-injector and the combustor wall

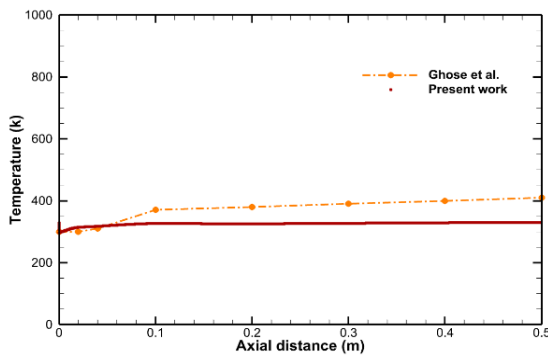
The considered is a temperature gradient along the combustor wall crucial component in terms of heat loss as well as the wall material's metallurgical barrier reduction. In a system that doesn't use pre-mixed fuels, like the combustor, one source of energy is radiation from the flame.

1. Figure 12 shows how the flow's reduced tangential momentum in this instance prevents the flame from spreading radially. On the other hand, a wall cooling impact results from the secondary air that is allowed into the combustor moving along the wall surface. A higher swirl intensifies the tangential motion, which spreads the flame and combines the hot combustion Secondary air is used to mix items. As a result, the secondary air cooling impact on walls is diminished.

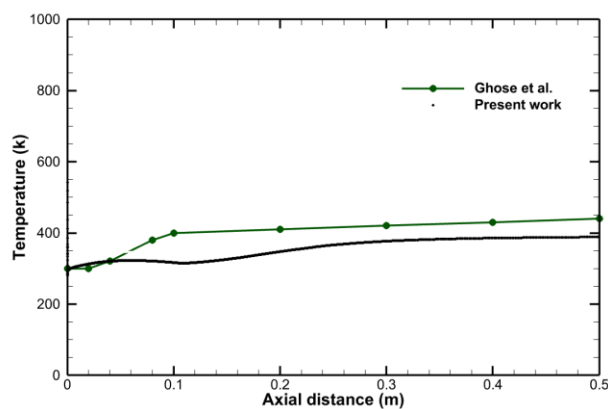
Figure 12 (a - d). Comparison between Ghose et al and Present work for Variation of temperature along the combustor wall at swirler vane angles of 40, 50, and 60.



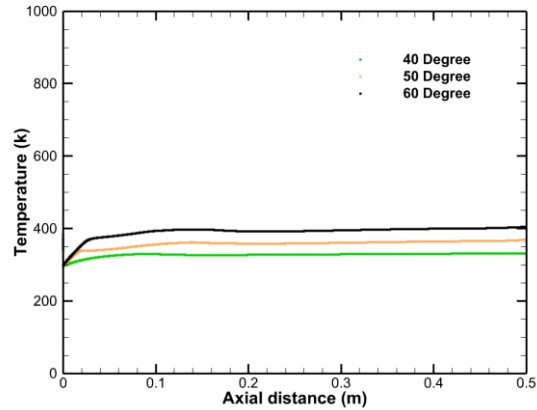
(a)



(b)



(c)



(d)

Therefore, even if the former scenario experiences less incoming radiation on the wall, when compared to a weaker swirl, The wall temperature is always greater along the whole length of the wall in the instance with a stronger swirl. In the high swirl instance, the greater wall temperature causes more heat loss through the exterior wall, which lowers the combustor's efficiency. The proportion of overall energy flow rate at the outflow to that at the intake is what is referred to as an efficiency (η) word. Table 4 contains the determined efficiency figures. It demonstrates that combustor efficiency falls down as the swirl number rises. The heat transmission to the fuel is a crucial factor in the combustor's performance.

Figure 12(a-d), demonstrates the temperature distributions on a swirler-injector plane with three degrees of swirl. The data shows that Case C, which has the largest swirl, has a much higher injector plane temperature than Cases A and B. This may be explained by the closeness At high swirl flow, the flame is closer to the injector, and the injector surface has a higher peak temperature. which is seen to not grow gradually with inlet swirl number. Instead, a modest swirl (Case B) of the main

flow was where the injector's lowest peak temperature was discovered. with a whirl in the main airflow. demonstrates the temperature distributions on a swirler-injector plane at three different degrees of swirl.

The data shows that Case C, which has the largest swirl, has a much higher injector plane temperature than Cases A and B. This could be explained by the closeness with high swirl flow of the flame to the injector and the higher peak temperature of the injector surface, which is seen to not grow gradually with inlet swirl number. Instead, a modest swirl (Case B) of the main flow was where the injector's lowest peak temperature was discovered. with a whirl in the main airflow. This is principally caused by an increase in the heat flux from incoming radiation higher on the vane whirl. However, compared to the injector, the swirler vane's peak temperature is substantially lower.

Table 4. Combustor efficiency at various cases

Cas	$\eta = \frac{\text{Total energy flow rate at combustor outlet}}{\text{Total energy flow rate at combustor inlet}} \%$
A	91.6
B	90.6
C	89.4

5. Conclusion

The impact of input swirl on kerosene spray combustion produced by in a cylindrical combustion chamber, a pressure swirl atomizer was investigated numerically in this work. a situation when the model's parameters have been properly tuned for use with kerosene flames. the nucleation and surface growth models must be greatly enhanced. Radiant heat transmission from the flame has been examined, with the contributions of participating gases taken into consideration.

For various swirl situations, Comparisons and studies have been done on the incidence radiation and temperature distributions on the combustor and the swirler-injector assembly wall. Also considered is the impact of swirl on the temperature distribution of the gas. The factor affecting the exit pattern is analyzed. Combustors in various situations have been researched. It has been shown that reducing the principal air flow swirl lengthens the flame. When the swirl becomes intense enough, the flame may even change its shape to an annular one following a vigorous recirculation. Furthermore, when there is a high swirl, the excess air is mixed in the flame zone, which decreases the peak temperature of the flame. over the flame, the species concentrations demonstrate that the CO₂ distribution in the combustor can accurately map the flame length. Any combustion-related emissions by directing the peak radiative zone downstream along the combustor wall, A longer flame with a lower swirl enhances incident radiation heat flux on the wall's surface. periphery. It is discovered that when the swirl increases, the temperature of the combustor wall rises, increasing heat loss and lowering combustor efficiency. On the other side, as the number of swirls grows, the incident radiation heat flux on the injector-swirler system does as well. It is discovered that the injector is the more important component since its temperature is significantly higher than that of the swirler vanes. The injector's peak temperature rises as the swirl flow increases due to the flame's closeness to the inlet plane. The exhaust gas temperature distribution becomes more uniform as the swirl grows and the combustor's flow mixing improves.

Reference

1. A.H. Lefebvre and D.R. Ballal, Gas Turbine Combustion: Alternative Fuels and Emissions CRC Press, Boca Raton, FL, 2010.
2. B.L. Koff, Gas turbine technology evolution: A designer's perspective, *J. Propul. Power* 20 (2004), pp. 577–595.
3. V.K. Arghode and A.K. Gupta, Development of high intensity CDC combustor for gas turbine engines, *Appl. Energy* 88 (2011), pp. 963–973
4. Düwel, I., et al., Experimental and numerical characterization of a turbulent spray flame. *Proceedings of the Combustion Institute*, 2007. 31(2): p. 2247-2255.
5. Mikami, M., S. Miyamoto, and N. Kojima, Counterflow diffusion flame with polydisperse sprays. *Proceedings of the Combustion Institute*, 2002. 29(1): p. 593-599.
6. Poorhoseinni, H., A. Saeedi, and M. Moghiman, Experimental and numerical investigation of the inlet air swirl angle effects on temperature profile and CO, NO pollutants. *Energy Engineering & Management*, 2012. 2(1): p. 32-39.
7. Zhou, L., X. Chen, and J. Zhang, Studies on the effect of swirl on soot formation in methane/air turbulent combustion. *Proceedings of the Combustion Institute*, 2002. 29(2): p. 2235-2242.
8. Zhou, Y., et al., An improved model to calculate radiative heat transfer in hot combustion gases. *Combustion Theory and Modelling*, 2020. 24(5): p. 829-851.
9. Bonatesta, F., et al. The influence of swirl ratio on soot quantity and distribution in the cylinder of a diesel engine. in *Third European Combustion Meeting ECM*. 2007.
10. Patel, V. and R. Shah, Experimental investigation on flame appearance and emission characteristics of LPG inverse diffusion flame with swirl. *Applied Thermal Engineering*, 2018. 137: p. 377-385.
11. Patel, V. and R. Shah, Effect of swirl and number of swirler vanes on combustion characteristics of methane inverse diffusion flame. *Journal of Mechanical Science and technology*, 2019. 33(4): p. 1947-1958.
12. Khelil, A., et al., Prediction of a high swirled natural gas diffusion flame using a PDF model. *Fuel*, 2009. 88(2): p. 374-381.
13. Khanafer, K. and S. Aithal, Fluid-dynamic and NO_x computation in swirl burners. *International Journal of Heat and Mass Transfer*, 2011. 54(23-24): p. 5030-5038.
14. Ilbas, M., The effect of thermal radiation and radiation models on hydrogen–hydrocarbon combustion modelling. *International Journal of Hydrogen Energy*, 2005. 30(10): p. 1113-1126.
15. Jones, W., S. Lyra, and S. Navarro-Martinez, Numerical investigation of swirling kerosene spray flames using large eddy simulation. *Combustion and Flame*, 2012. 159(4): p. 1539-1561.
16. Yılmaz I. Effect of swirl number on combustion characteristics in a natural gas diffusion flame. *J Energy Resour Technol* 2013;135:1e8..
17. Khanafer, K., & Aithal, S. M. (2011). Fluid-dynamic and NO_x computation in swirl burners. *International Journal of Heat and Mass Transfer*, 54(23-24), 5030-5038.

18. Datta, A., & Som, S. K. (1999). Combustion and emission characteristics in a gas turbine combustor at different pressure and swirl conditions. *Applied Thermal Engineering*, 19(9), 949-967.
19. Rohani, B. and K.M. Saqr, Effects of hydrogen addition on the structure and pollutant emissions of a turbulent unconfined swirling flame. *International Communications in Heat and Mass Transfer*, 2012. 39(5): p. 681-688.
20. D. Joung and K.Y. Huh, Numerical Simulation of Non-Reacting and Reacting Flows in a 5 MW Commercial Gas Turbine Combustor, *ASME Turbo Expo 2009: Power for Land, Sea, and Air*, Orlando, FL, June 8–12, 2009
21. C.E. Choi and S.W. Baek, Numerical analysis of a spray combustion with nongray radiation using weighted sum of gray gases model, *Combust. Sci. Technol.* 115 (1996), pp. 297–315.
22. S. Pope, " Combustion Modelling using Probability Density Function Methods," *Numerical Approaches to Combustion Modelling*, Prog. Astronaut. Aeronaut, AIAA, 1991.
23. S. Morsi and A. Alexander , "An investigation of particle trajectories in two-phase systems," *Journal of Fluid mechanics*, vol. 55, no. 2, pp. 193-208, 1972.
24. E. H. Chui and G. D. Raithby. "Computation of Radiant Heat Transfer on a Non- Orthogonal Mesh Using the Finite-Volume Method". *Numerical Heat Transfer, Part B*. 23. 269–288. 1993.
25. G. D. Raithby and E. H. Chui. "A Finite-Volume Method for Predicting a Radiant Heat Transfer in Enclosures with Participating Media". *J. Heat Transfer*. 112. 415–423. 1990.
26. J. Y. Murthy and S. R. Mathur. "A Finite Volume Method For Radiative Heat Transfer Using Unstructured Meshes". AIAA-98-0860. January 1998.
27. S. R. Mathur and J. Y. Murthy. "Coupled ordinates method for multigrid acceleration of radiation calculations". *J. of Thermophysics and Heat Transfer*. 13(4). 1783-1785. 1999.
28. S. R. Mathur and J. Y. Murthy. "Coupled ordinates method for multigrid acceleration of radiation calculations". *J. of Thermophysics and Heat Transfer*. 13(4). 1783-1785. 1999.
29. P. Cheng. "Two-Dimensional Radiating Gas Flow by a Moment Method". *AIAA Journal*. 2. 1662–1664.
30. R. Siegel and J. R. Howell. "Thermal Radiation Heat Transfer. Hemisphere Publishing Corporation, Washington DC. 1992.
31. P. Ghose, J. Patra, A. Datta, and A. Mukhopadhyay, Effect of air flow distribution on soot formation and radiative heat transfer in a model liquid fuel spray combustor firing kerosene, *Int. J. Heat Mass Transfer* 74 (2014), pp. 143–155.
32. ANSYS Fluent 15.0 user's guide, 2013, software available on www.ansys.com.
33. Ghose, P., Patra, J., Datta, A., & Mukhopadhyay, A. (2016). Prediction of soot and thermal radiation in a model gas turbine combustor burning kerosene fuel spray at different swirl levels. *Combustion Theory and Modelling*, 20(3), 457-485.